Search for neutrino counterparts to the gravitational wave sources from LIGO/Virgo O3 run with the ANTARES detector

The ANTARES collaboration

E-mail: antares.spokesperson@in2p3.fr

Abstract. Since 2015 the LIGO and Virgo interferometers have detected gravitational waves from almost one hundred coalescences of compact objects (black holes and neutron stars). This article presents the results of a search performed with data from the ANTARES telescope to identify neutrino counterparts to the gravitational wave sources detected during the third LIGO/Virgo observing run and reported in the catalogues GWTC-2, GWTC-2.1, and GWTC-3. This search is sensitive to all-sky neutrinos of all flavours and of energies $> 100\,\text{GeV}$, thanks to the inclusion of both track-like events (mainly induced by ν_μ charged-current interactions) and shower-like events (induced by other interaction types). Neutrinos are selected if they are detected within $\pm 500\,\text{s}$ from the GW merger and with a reconstructed direction compatible with its sky localisation. No significant excess is found for any of the 80 analysed GW events, and upper limits on the neutrino emission are derived. Using the information from the GW catalogues and assuming isotropic emission, upper limits on the total energy $E_{\text{tot},\nu}$ emitted as neutrinos of all flavours and on the ratio $f_\nu = E_{\text{tot},\nu}/E_{\text{GW}}$ between neutrino and GW emissions are also computed. Finally, a stacked analysis of all the 72 binary black hole mergers (respectively the 7 neutron star-black hole merger candidates) has been performed to constrain the typical neutrino emission within this population, leading to the limits: $E_{\text{tot},\nu} < 4.0 \times 10^{53}\,\text{erg}$ and $f_\nu < 0.15$ (respectively, $E_{\text{tot},\nu} < 3.2 \times 10^{53}\,\text{erg}$ and $f_\nu < 0.88$) for E^{-2} spectrum and isotropic emission. Other assumptions including softer spectra and non-isotropic scenarios have also been tested.

Contents

1 Introduction

Since the first detection of gravitational waves (GWs) from compact binary mergers in 2015 [1], GW interferometers have opened a new window on the Universe, complementary to the ones already being explored with other cosmic messengers (cosmic rays, photons, neutrinos). These capabilities have already allowed the association of the GW signal GW170817 emitted by the merger of a binary neutron star system with the emission of a short gamma-ray burst (GRB), GRB 170817A, detected by Fermi and INTEGRAL in gamma rays, and the related afterglow across a wider range of the electromagnetic spectrum [2].

Neutrinos are also expected to be emitted from the relativistic outflows that characterise such mergers: see e.g., [3] for binary neutron star (BNS) mergers, [4] for neutron star-black hole (NSBH) mergers, and [5] for binary black hole (BBH) mergers. Previous searches performed with ANTARES [6], Baikal-GVD [7], IceCube [8], and Super-Kamiokande [9] have not been able to identify an excess of neutrinos and upper limits have been reported.

This article presents an updated search using the latest GW catalogues covering detections in 2019–2020 and the ANTARES data from the same period. Besides the follow-up of individual events, performed in the same way as in previous publications, first population studies are also presented by carrying out a stacking analysis for binary mergers of the same nature and taking advantage of the extensive catalogue reported by the GW community.

1.1 The GW catalogues

This paper focuses on GW sources detected during the third observing run (O3) of the LIGO and Virgo detectors and reported in the following official LIGO/Virgo catalogues:

- GWTC-2 [10]: this catalogue reports detections made during the first half of O3 (April–September 2019). It contains 39 candidates, including 1 BNS, 2 NSBH, and 36 BBH events.

- GWTC-2.1 [11]: this is an update of GWTC-2, with 8 additional events not reported in the previous catalogue and that have a high probability of astrophysical origin. The catalogue also includes a larger selection of $\sim 1.2\,\mathrm{k}$ events with a false alarm rate of less than 2 per day but lower astrophysical probability, which are not considered in this analysis.

- GWTC-3 [12]: this catalogue covers the second half of O3 (November 2019–March 2020) and contains 35 objects, including 4 NSBH candidates. Seven marginal candidates that do not fully satisfy the criteria for an astrophysical origin are also reported, of which only GW200105_162426 is kept as it has also been reported independently as a plausible NSBH candidate [13].

For each of these objects, the LIGO-Virgo collaboration provides a FITS file [14] with the timing of the merger t_{GW} and the constraints on the source direction Ω as a skymap $\mathcal{P}(\Omega)$, as well as posterior samples containing all the correlations between source direction Ω, luminosity distance estimate D_L, and other source parameters such as the masses of the two merging objects $m_{1,2}$ (with the convention $m_1 > m_2$), the energy radiated in gravitational waves E_{GW} (defined as the difference between the estimated mass of the final object and the sum of the masses of the initial objects), and the inclination between the total angular momentum and the line-of-sight θ_{jn}. The classification among the different categories is made based on the mass estimates: BNS if $m_2 < m_1 < 3\,\mathrm{M}_\odot$, NSBH if $m_2 < 3\,\mathrm{M}_\odot < m_1$, BBH otherwise. When considering the different catalogues, 83 objects are selected, including 1 BNS and 7 NSBH candidates.

1.2 The ANTARES telescope

The ANTARES neutrino telescope [15], located in the depths of the Mediterranean Sea, offshore from Toulon (France), has been operating in its final configuration between May 2008 and February 2022. It was composed of an array of 885 photomultiplier tubes (PMTs) enclosed in pressure-proof glass spheres, arranged in triplets over 12 vertical lines, spaced by $\sim 70\,\mathrm{m}$ and anchored at a depth of $\sim 2475\,\mathrm{m}$.

The PMTs detect the Cherenkov light induced by relativistic charged particles originating in the interaction of a neutrino with matter surrounding the detector; the space and time pattern of PMT signals (or hits) allows the neutrino properties (direction and energy) to be inferred. Charged-current interactions of muon (anti-)neutrinos are characterised by the presence of a long muon track; the typical angular resolution for such events is $< 1°$ for $E_\nu > 100\,\mathrm{GeV}$ [16]. Other types of neutrino interactions only produce hadronic (and, in the case of ν_e charged-current interactions, electromagnetic) showers, with a more localised light deposit and compact topology. Despite the shorter lever arm with respect to the muon tracks, ANTARES still achieved a median angular resolution of a few degrees for the neutrino

direction [17]. In the following, the two event categories described above are referred to as the track and shower samples respectively.

ANTARES data were organised in consecutive runs of at most twelve hours. The present analysis uses data from 2019 and 2020 to identify neutrino counterparts to the GW emissions described in section 1.1. A larger dataset including data from January 2018 to December 2020 is used for background estimation.

Several searches for neutrino counterparts to GW events with ANTARES have been carried out in the past. These studies were limited to event-by-event follow-ups and reported null results. See [18] for GW170104, [19] for GW170817, and [6] for other O2 events.

2 Analysis method

This search focuses on the selection of neutrino events in a time window of $1000\,\mathrm{s}$ centred on the GW emission time t_{GW}, as motivated in [20], and in the region $\mathcal{R}_{90}$ containing 90% of the source localisation probability, as built directly from the GW 2D skymaps $\mathcal{P}(\Omega)$. As the reconstructed event direction does not match the true neutrino direction perfectly due to the scattering angle and the finite detector resolution, this region of interest (RoI) is extended by an angle α to account for these effects, meaning that an event with direction $\boldsymbol{x}$ would be selected if $\min_{\boldsymbol{d}\in\mathcal{R}_{90}}(\arccos{(\boldsymbol{x}\cdot\boldsymbol{d})}) \leq \alpha$. This extended angle α is a free parameter of the analysis, whose choice is based on the optimisation method described below.

The ANTARES events are divided into four categories according to whether they are classified as tracks or showers and whether their reconstructed direction is upgoing or downgoing, each case based on a specific selection and optimisation procedure, as described in sections 2.1 and 2.2.

The reconstructed data are largely dominated by atmospheric muons. A selection is then applied to reduce it to an expected number of events $B = 2.7 \times 10^{-3}$, such that the detection of one event would correspond to a 3σ excess (3σ condition). This condition is separately set for each category. For a given GW, the background expectation is estimated using the dataset from 2018 to 2020. Only runs with similar data-taking conditions as the ones during the ANTARES run r_{GW} overlapping with the GW time, characterised by the mean burst fraction,[1] are selected. As illustrated in the left panel of figure 1, this procedure is found to allow for a proper estimate of the background while ensuring a better characterisation of the tails of the distribution as compared to a statistically-limited estimation using only the data from the run r_{GW}.

A dedicated Monte Carlo (MC) simulation [22] has been produced to be used in this optimisation process. Simulations are done on a run-by-run basis, where each run has a specific simulation to reproduce the particular environmental and detector conditions during this run. For GW events with precise sky localisation ($\mathcal{R}_{90}$ region smaller than $3000\,\mathrm{deg}^2$), additional neutrinos generated solely within this region have also been produced to accurately estimate the corresponding detector acceptance for an $E^{-\gamma}$ spectrum ($= \int A_{\mathrm{eff}}(E)E^{-\gamma}\mathrm{d}E$, where $A_{\mathrm{eff}}(E)$ is the effective area). More details about the detector acceptance for a given neutrino spectrum are in [23].

The final cuts are optimised to ensure that the expected number of selected background events after all cuts is fulfilling the 3σ condition defined above.

---

[1]This quantity is defined by estimating how often, in a given run, the PMT counting rate is more than 20% higher than the baseline value for this run. This quantity has been found to be correlated with the detector noise level, whose evolution is mainly driven by deep-sea bioluminescent emissions [21].

(a) Estimation of the background. (b) Optimisation of the cuts.
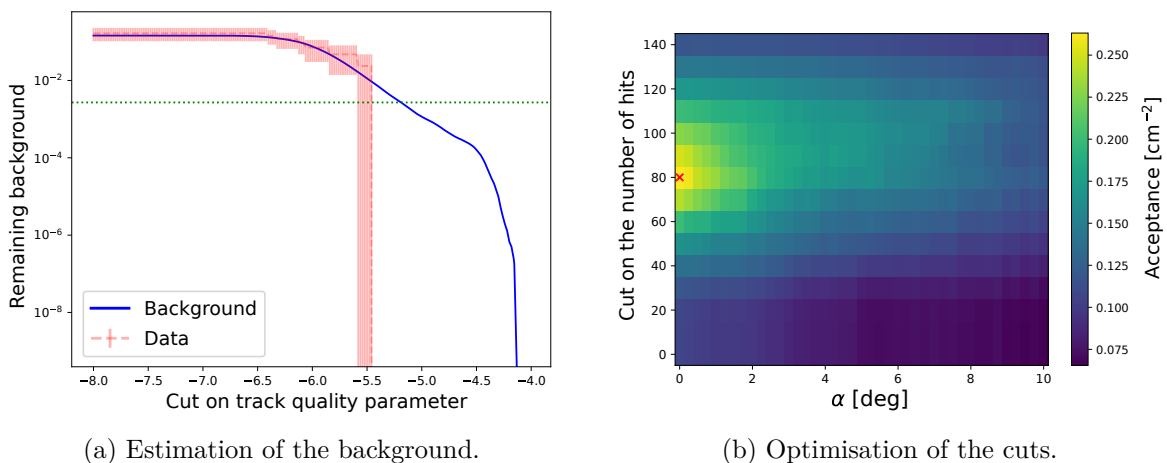
Figure 1. Illustration of the analysis procedure for the downgoing track category for GW190521. The left panel shows the expected remaining background after varying cuts on the track quality parameter Λ: the blue curve shows the estimation based on the procedure described in the previous paragraphs, the red histogram shows the background estimated using only the ANTARES 12-hour run containing the signal time window with its statistical uncertainty, and the dotted line is the required background to ensure the 3σ condition. The right panel shows the average acceptance, assuming an E^{-2} neutrino spectrum, as a function of the cut on the number of hits and the value of α. For each bin, the cut on Λ is fixed to the value that satisfies exactly the 3σ condition. The optimal working point, maximising the acceptance, is indicated by the red cross.

2.1 Track event selection

The track selection procedure is adapted from the one presented in [18]. The upgoing and downgoing (respectively with reconstructed incoming direction below or above the horizon) event selections are different, as the latter is more likely to be contaminated by the atmospheric muon background and needs extra care.

For upgoing tracks, a cut on the track reconstruction quality parameter, Λ [24], is applied. The values of α and of the cut on Λ are optimised by ensuring the 3σ condition described above, as well as maximising the signal acceptance in the hypothesis of an E^{-2} spectrum. For downgoing events, the procedure is similar except that an additional cut on the number of hits employed for the reconstruction is also applied, as illustrated in the right panel of figure 1.

2.2 Shower event selection

The selection steps for neutrino interactions yielding showering events are similar to the ones presented in [6]. Events must be contained within the detector and must not be classified as a track by the selection described in the previous section. The discrimination between neutrinos and atmospheric muons is achieved thanks to an extended likelihood ratio $\mathcal{L}_\mu$ defined by comparing the neutrino and muon hypotheses for each hit associated with the shower on the basis of its deposited charge, timing, and distance to the reconstructed shower position [17]. Another parameter is used to further reduce the background contamination: for upgoing events, this parameter is defined from a Random Decision Forest (RDF) classifier [25] while the downgoing selection exploits the number of hits used in the event fitting.
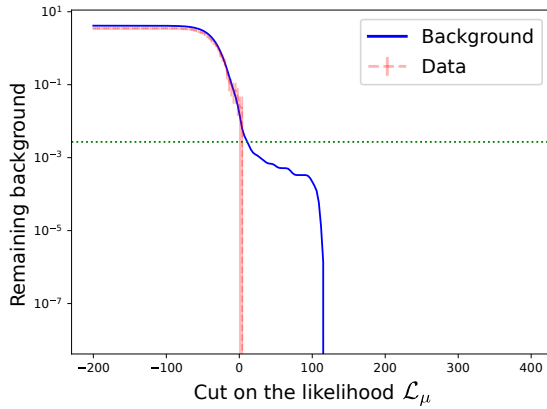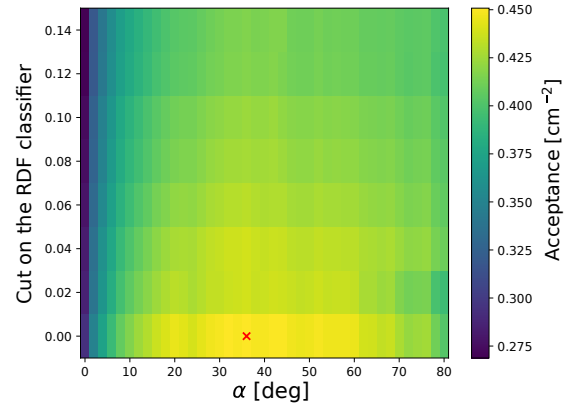
(a) Estimation of the background.   (b) Optimisation of the cuts.

Figure 2. Illustration of the analysis procedure for the downgoing shower category for GW190521. The left panel shows the expected remaining background after varying cuts on $\mathcal{L}_\mu$ with the same colour code and line style as in figure 1. The right panel shows the average acceptance, assuming an E^{-2} neutrino spectrum, as a function of the cut on the RDF classifier and the value of α. For each bin, the cut on $\mathcal{L}_\mu$ is fixed to the value that satisfies exactly the 3σ condition. The optimal working point, maximising the acceptance, is indicated by the red cross.

As for the track selection, the values of the cuts on these parameters and on the extension of the RoI α are optimised to ensure the 3σ condition and to maximise the acceptance, as illustrated in figure 2.

2.3 Detector systematics

Several systematic effects may affect the detector performance, hence the obtained constraints on the neutrino emission. Three sources of uncertainty, found to be the dominant effects as already described e.g. in [6], are taken into account and evaluated independently for the four event categories (track/showers upgoing/downgoing):

- The first one is related to the uncertainty on the PMT photon detection efficiency and on the water absorption length; the related uncertainties have been re-evaluated by varying these two quantities within a typical interval of ±10% in dedicated MC simulations and estimating the overall impact on the signal acceptance.

- The second source is linked to the capability of the run-by-run MC simulations to properly reproduce data conditions; the related error is estimated by comparing the variability of event rates between data and simulations.

- The last effect is the combined statistical and systematic uncertainty on the background expectation. The related uncertainty is obtained by varying the list of similar runs employed for its estimation.

The total uncertainties on the acceptance related to the first two sources are 18%, 14%, 21%, and 19% respectively for the upgoing tracks, downgoing tracks, upgoing showers, and downgoing showers. The overall uncertainty on the background is about 20% for all event categories.

3 Statistical analysis

For each GW event, the number of observed neutrino candidates in time and spatial coincidence in each category can be converted into a significance of the observation using Poisson statistics. In the absence of any excess of neutrino events with respect to the background expectation, upper limits on the neutrino emission are calculated. In the following section, several assumptions are made:

(i) The source localisation is supposed to be within $\mathcal{R}_{90}$ (as this is the region for which the selection has been optimised). Therefore, the GW posterior samples are restricted to those with $\Omega \in \mathcal{R}_{90}$ and the final constraints neglect the chances for the actual source to be localised in the rest of the sky.

(ii) There is equipartition between the neutrino flavours at Earth due to the averaging of oscillations over astronomical distances [26], starting from $\nu_e : \nu_\mu : \nu_\tau = 1 : 2 : 0$ at production. This allows reporting limits on the all-flavour neutrino emission.

(iii) The neutrino energy spectrum is described by a single power law $\mathrm{d}N/\mathrm{d}E = \phi \cdot (E/\mathrm{GeV})^{-\gamma}$ where ϕ is expressed in units of $\mathrm{GeV}^{-1}\,\mathrm{cm}^{-2}$ and γ is the spectral index. The nominal case is $\gamma = 2$ (E^{-2} spectrum).

The ANTARES acceptance is estimated using the MC simulations described in section 2. It depends on the shape of the assumed neutrino spectrum (characterised by γ), on the source direction Ω, and on the event category c. It is averaged over the neutrino flavours and can be decomposed into a normalisation factor and a direction-dependent component: $\mathcal{A}_\gamma^{(c)}(\Omega) = a_\gamma^{(c)} \cdot f_\gamma^{(c)}(\Omega)$.

3.1 Constraints on the neutrino flux

This section presents the limits on the overall flux normalisation ϕ obtained for an all-flavour emission with $\gamma = 2$. The cut-and-count analysis described in the previous sections corresponds to a Poisson likelihood

$$\mathcal{L}\left(\{N^{(c)}\}; \{B^{(c)}\}, \{a_\gamma^{(c)}\}, \Omega, \phi, \gamma\right) = \prod_{c \in \mathcal{C}} \mathrm{Poisson}\left(N^{(c)}; B^{(c)} + \phi \cdot a_\gamma^{(c)} \cdot f_\gamma^{(c)}(\Omega)\right), \qquad (3.1)$$

where $N^{(c)}$ (resp. $B^{(c)}$) is the observed (resp. background-expected) number of events in each category, and the product is performed over the set of four event categories ($c \in \mathcal{C}$, $\mathcal{C} = \{$upgoing tracks, downgoing tracks, upgoing showers, downgoing showers$\}$). Given the selection optimisation presented in section 2, the value of $B^{(c)}$ is fixed to 2.7×10^{-3}, independently for all categories.

A Bayesian method is employed to obtain constraints on the neutrino flux normalisation ϕ starting from this likelihood. A flat prior on ϕ is employed, the systematic uncertainties described in section 2.3 are encoded in Gaussian priors on $B^{(c)}$ and on $a_\gamma^{(c)}$ with the standard deviations corresponding to the uncertainties reported there, and the GW skymap $\mathcal{P}(\Omega)$ is used as a prior on Ω.

The obtained posterior probability is then marginalised over all the nuisance parameters (background, acceptance, direction) by using MC integration techniques: toy samples (t.s.) are generated with values of $B^{(c)}$ and $a_\gamma^{(c)}$ following the priors, and the posterior samples

from GW catalogues can be used directly for the sampling of Ω. The marginalised posterior probability distribution is computed as

$$P(\phi) = C \sum_{s \in \mathrm{t.s.}} \mathcal{L}\left(\{N^{(c)}\}; \{B^{(c)}\}_s, \{a_\gamma^{(c)}\}_s, \Omega_s, \phi, \gamma\right), \tag{3.2}$$

where C is a normalisation constant that can be determined numerically by ensuring $\int_0^\infty P(\phi)\mathrm{d}\phi = 1$. The 90% upper limit ϕ_{90} is finally obtained by solving $\int_0^{\phi_{90}} P(\phi)\mathrm{d}\phi = 0.90$.

3.2 Constraints on the total energy

Similarly to the incoming neutrino flux on Earth, one may also constrain the total energy $E_{\mathrm{tot},\nu}$ emitted in neutrinos, correcting for the source distance. This can be done under a specific assumption on the spatial distribution of the neutrino emission around the source, e.g., either isotropic or collimated into a jet. One may also consider the ratio between the total energy emitted in neutrinos and the energy E_{GW} radiated in GW: $f_\nu = E_{\mathrm{tot},\nu}/E_{\mathrm{GW}}$.

Isotropic emission. In the case of a source emitting isotropically, the total energy emitted in neutrinos can be computed as

$$E_{\mathrm{tot},\nu}^{\mathrm{iso}} = 4\pi D_L^2 \int_{E_{\min}}^{E_{\max}} E \times \frac{\mathrm{d}N}{\mathrm{d}E}\,\mathrm{d}E = \phi \times 4\pi D_L^2 \int_{E_{\min}}^{E_{\max}} E^{-\gamma+1}\,\mathrm{d}E, \tag{3.3}$$

where D_L is the source luminosity distance, and $E_{\min}$, $E_{\max}$ are the integration bounds. For this analysis, these bounds are fixed to $E_{\min} = 5\,\mathrm{GeV}$ and $E_{\max} = 10^8\,\mathrm{GeV}$, which is the typical range where the emission is expected in most of the models (e.g., [27]).

Since the total energy $E_{\mathrm{tot},\nu}^{\mathrm{iso}}$ is proportional to the flux normalisation ϕ, the likelihood from equation (3.1) can be rewritten in terms of $E_{\mathrm{tot},\nu}^{\mathrm{iso}}$ instead of ϕ. The marginalised posterior probability and the upper limits are obtained similarly, where the luminosity distance is also extracted from GW posterior samples to be used in MC integration toy samples and a flat prior on $E_{\mathrm{tot},\nu}^{\mathrm{iso}}$ is assumed. A similar rewriting is possible to obtain the limits on $f_\nu^{\mathrm{iso}} = E_{\mathrm{tot},\nu}^{\mathrm{iso}}/E_{\mathrm{GW}}$. This is a relevant parameter if it is assumed that the total energy emitted in neutrinos scales with the GW emission.

Non-isotropic scenarios. One may also consider the total energy $E_{\mathrm{tot},\nu}$ for a given non-isotropic model, and the corresponding likelihoods and posteriors can be written using the relevant GW parameters for the marginalisation. For non-isotropic emission, a simple von Mises [28] jet model is considered:

$$p(\theta; \omega) = \frac{1}{4\pi\omega^2 \sinh(1/\omega^2)} \times \exp(\cos\theta/\omega^2), \tag{3.4}$$

where ω characterises the jet opening and θ is the angle with respect to the jet central direction. In the following, the jet is assumed to be collinear with the total angular momentum of the merger, such that $\theta = \theta_{\mathrm{jn}}$ from the GW data release. The total energy emitted in neutrinos for a power-law spectrum is then

$$E_{\mathrm{tot},\nu} = \phi \times 2\pi D_L^2 \int_{E_{\min}}^{E_{\max}} E^{-\gamma+1}\,\mathrm{d}E \times \frac{\int p(\theta; \omega)\sin\theta\,\mathrm{d}\theta}{p(\theta_{\mathrm{jn}}; \omega)}, \tag{3.5}$$

where the last term is the correction corresponding to the jet visibility from Earth (in the isotropic case, this term would be 2, such that the equation (3.3) is retrieved). For a given jet opening ω, the limits on $E_{\mathrm{tot},\nu}$ or the corresponding f_ν may be derived as described in the isotropic case, including θ_{jn} variable in MC integration toy samples.

3.3 Stacking analysis

The GW catalogues published by LIGO/Virgo may contain populations of sources with similar neutrino emissions, which could be more efficiently constrained by performing stacking analyses. A first version of such an analysis is presented here with two categories of GW events: the 72 BBH mergers on one side and the 7 NSBH mergers on the other. While differing in its precise implementation in this study, the method follows the ideas initially presented in [29] and already applied in [9] with Super-Kamiokande data.

The stacking approach assumes that all objects in the selected population have the same emission, either in terms of total energy $E_{\text{tot},\nu}$ or of f_ν. In the non-isotropic scenarios, GW sources in a given population may have different jet inclinations but the shape of the jet (the parameter ω for the von Mises model) is considered to be the same for all the objects.

Assuming a flat prior on the signal parameters and considering all observations as independent, the posterior distribution for a given population $\mathcal{S}$ may be written as

$$P_{\mathcal{S}}(X;Y) = C \prod_{i \in \mathcal{S}} P_i(X;Y,Z_i), \tag{3.6}$$

where C is a normalisation constant, X is the signal parameter to be constrained ($E_{\text{tot},\nu}$ or f_ν), Y may denote potential common parameters (such as ω), and Z_i represents the parameters which may differ from one GW event to another within $\mathcal{S}$. Upper limits on X can then be obtained with the same method as before.

The stacking approach is particularly interesting to constrain the non-isotropic models, as is detailed in the next section.

4 Results

A total of 80 GW events out of the 83 observed during O3, including all candidates involving at least one neutron star, can be associated with exploitable ANTARES data.

For each follow-up, the neutrino event selection is optimised according to the procedure described in section 2 and the final number of selected events in time and spatial coincidence with the GW event in each category is extracted. No event has been selected for any of the follow-ups, which is fully compatible with the expected background $\sum_{i \in \text{GWs}} \sum_{c \in \mathcal{C}} B_i^{(c)} \sim 0.82$. Therefore, only upper limits on the neutrino flux and other related quantities are reported in the following.

Table 1 displays the 90% upper limits on the incoming all-flavour neutrino emission assuming an E^{-2} spectrum, along with GW information, for the events initially reported in the GWTC-2 catalogue. Similarly, the results for the events in GWTC-2.1 and GWTC-3 are presented in table 2 and table 3, respectively. The all-flavour flux limits assuming an E^{-2} spectrum stands mostly between 4 and $60\,\text{GeV}\,\text{cm}^{-2}$.

Figure 3 shows the limits on the total energy emitted in all-flavour neutrinos and on $f_\nu^{\text{iso}} = E_{\text{tot},\nu}^{\text{iso}}/E_{\text{GW}}$, assuming isotropic emission, for events from the three catalogues. The limits range from 10^{54} to 10^{59} erg and are mostly following the expected D_L^2 trend.

Population studies are performed by stacking (a) all 72 BBH events, and (b) the 7 NSBH candidates. Figure 4 shows the stacked upper limits on the typical total energy emitted in neutrinos (or the ratio f_ν) within these two categories, considering jetted emission with the von Mises model (as a function of the jet opening ω) as well as for isotropic emission, and assuming $E^{-\gamma}$ spectra with $\gamma = 2.0, 2.5, 3.0$.

GW name	Type	D_L	$\mathcal{R}_{90}$ area	Upper limits on neutrino emission		
				$E^2\mathrm{d}N/\mathrm{d}E$	$E_{\mathrm{tot},\nu}^{\mathrm{iso}}$	f_ν^{iso}
		Mpc	deg^2	GeV cm^{-2}	erg	
GW190412	BBH	734	24	1.8×10^1	3.4×10^{55}	1.7×10^1
GW190413_052954	BBH	4190	1383	6.4×10^1	1.8×10^{57}	3.7×10^2
GW190413_134308	BBH	5182	520	5.4×10^0	5.9×10^{56}	9.1×10^1
GW190421_213856	BBH	3166	1023	1.0×10^1	3.4×10^{56}	6.1×10^1
GW190424_180648	BBH	2568	25902	4.6×10^1	1.2×10^{57}	2.0×10^2
GW190425	BNS	157	9881	2.1×10^1	2.3×10^{54}	8.6×10^0
GW190426_152155	NSBH	377	1392	2.6×10^1	2.4×10^{55}	8.7×10^1
GW190503_185404	BBH	1527	97	4.4×10^0	4.5×10^{55}	7.7×10^0
GW190512_180714	BBH	1462	229	4.6×10^0	4.0×10^{55}	1.6×10^1
GW190513_205428	BBH	2190	494	6.3×10^0	9.0×10^{55}	2.3×10^1
GW190514_065416	BBH	4988	2402	1.1×10^1	1.1×10^{57}	2.4×10^2
GW190517_055101	BBH	2270	468	1.8×10^1	6.7×10^{56}	9.5×10^1
GW190519_153544	BBH	3023	770	1.2×10^1	7.2×10^{56}	7.3×10^1
GW190521	BBH	4567	937	1.2×10^1	9.6×10^{56}	7.3×10^1
GW190521_074359	BBH	1244	509	1.8×10^1	9.9×10^{55}	1.7×10^1
GW190527_092055	BBH	3563	3795	4.1×10^1	4.6×10^{57}	6.4×10^2
GW190602_175927	BBH	3138	721	5.4×10^0	2.4×10^{56}	2.6×10^1
GW190620_030421	BBH	3211	6674	2.9×10^1	1.4×10^{57}	1.6×10^2
GW190630_185205	BBH	956	1275	2.7×10^1	9.9×10^{55}	2.2×10^1
GW190701_203306	BBH	2152	47	6.1×10^0	9.8×10^{55}	1.3×10^1
GW190706_222641	BBH	5184	611	9.7×10^0	1.3×10^{57}	1.3×10^2
GW190707_093326	BBH	791	1343	2.4×10^1	7.1×10^{55}	4.5×10^1
GW190708_232457	BBH	888	13701	2.6×10^1	7.6×10^{55}	3.2×10^1
GW190719_215514	BBH	4786	2281	5.2×10^3	2.1×10^{59}	3.0×10^4
GW190720_000836	BBH	906	517	2.5×10^1	6.0×10^{55}	3.6×10^1
GW190727_060333	BBH	3609	861	1.6×10^1	8.7×10^{56}	1.4×10^2
GW190731_140936	BBH	4034	3042	1.8×10^1	1.4×10^{57}	2.5×10^2
GW190803_022701	BBH	3750	1538	2.2×10^1	9.7×10^{56}	1.9×10^2
GW190814	NSBH	241	20	4.6×10^0	9.5×10^{53}	2.2×10^0
GW190828_063405	BBH	2160	525	8.7×10^0	1.4×10^{56}	2.6×10^1
GW190828_065509	BBH	1658	637	7.1×10^0	9.6×10^{55}	4.5×10^1
GW190909_114149	BBH	4924	4071	3.0×10^1	3.7×10^{57}	7.1×10^2
GW190910_112807	BBH	1670	10014	2.2×10^1	3.8×10^{56}	6.3×10^1
GW190915_235702	BBH	1715	386	5.4×10^0	7.2×10^{55}	1.5×10^1
GW190924_021846	BBH	572	379	8.9×10^0	1.1×10^{55}	1.1×10^1
GW190929_012149	BBH	3901	1846	1.4×10^1	1.4×10^{57}	2.3×10^2
GW190930_133541	BBH	786	1829	1.5×10^1	3.5×10^{55}	2.4×10^1

Table 1. Summary of GWTC-2 follow-up results. The first four columns summarise the relevant GW information [10], including the most probable merger type, the estimated median luminosity distance D_L, and the size of the region $\mathcal{R}_{90}$ containing 90% of the localisation probability, while the three last ones show the 90% upper limits on the all-flavour neutrino emission assuming an E^{-2} spectrum (this work), in terms of the flux normalisation $E^2\mathrm{d}N/\mathrm{d}E$, the total isotropic energy $E_{\mathrm{tot},\nu}^{\mathrm{iso}}$, and the ratio f_ν^{iso}.

GW name	Type	Distance	$\mathcal{R}_{90}$ area	Upper limits on neutrino emission		
				$E^2 \mathrm{d}N/\mathrm{d}E$	$E^{\mathrm{iso}}_{\mathrm{tot},\nu}$	f^{iso}_{ν}
		Mpc	deg^2	GeV cm^{-2}	erg	
GW190403_051519	BBH	10853	4250	2.9×10^1	1.7×10^{58}	1.8×10^3
GW190426_190642	BBH	5995	8030	3.6×10^1	5.4×10^{57}	3.5×10^2
GW190725_174728	BBH	1128	2435	2.5×10^1	1.5×10^{56}	1.3×10^2
GW190805_211137	BBH	7235	3089	4.1×10^1	9.9×10^{57}	1.5×10^3
GW190916_200658	BBH	6180	3573	3.4×10^1	7.0×10^{57}	1.2×10^3
GW190917_114630	NSBH	741	1801	1.2×10^1	2.8×10^{55}	7.8×10^1
GW190925_232845	BBH	973	955	6.7×10^0	2.4×10^{55}	7.7×10^0
GW190926_050336	BBH	5073	2212	5.6×10^1	9.6×10^{57}	2.0×10^3

Table 2. Same as table 1 for the additional events in the GWTC-2.1 catalogue [11].
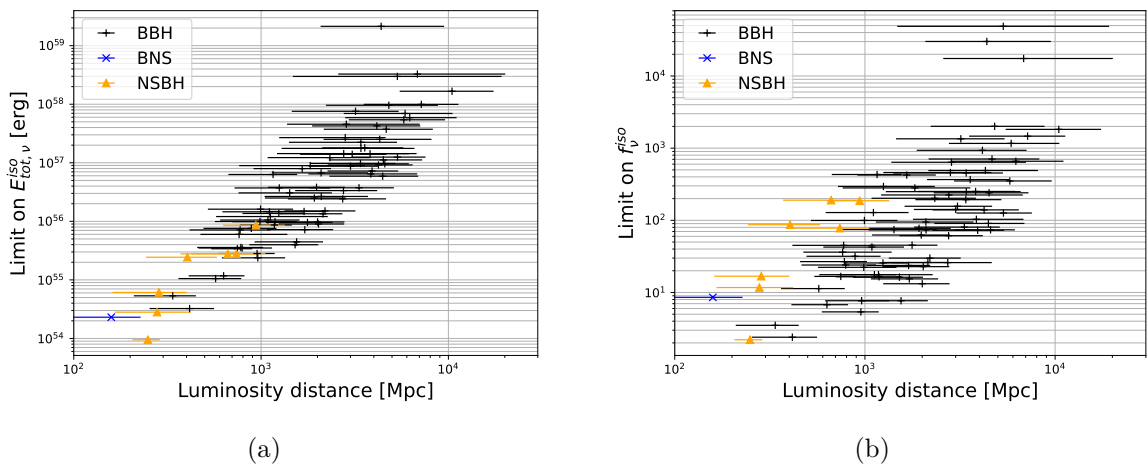
Figure 3. 90% upper limits on the total energy $E^{\mathrm{iso}}_{\mathrm{tot},\nu}$ emitted in neutrinos of all flavours (left) and on $f^{\mathrm{iso}}_{\nu} = E^{\mathrm{iso}}_{\mathrm{tot},\nu}/E_{\mathrm{GW}}$ (right) as a function of the source luminosity distance, assuming an E^{-2} spectrum and isotropic emission. The horizontal bars indicate the $5-95\%$ range of the luminosity distance estimate, and the markers/colours correspond to the different source categories.

For individual follow-ups, as θ_{jn} is not strongly constrained by GW detections, von Mises emission constraints are mainly dominated by geometrical effects: when the jet opening angle is narrow, there is a very small chance that the Earth is aligned with the jet, while a wide opening leads to a larger spread in total energy, which is hence more difficult to constrain. The limits on the total energy as a function of the jet opening are thus expected to show a typical parabola shape corresponding to a trade-off between these two effects, as illustrated by the envelope of individual limits shown in figure 4. While the individual results for jetted emission are of little interest due to these limitations, the stacking analysis of this scenario yields some benefit as, statistically, some of the sources are expected to point toward Earth for large enough jet opening angles. This can be seen on figure 4, in particular for the BBH event sample, with the largest statistics, where the neutrino emission can be constrained down to opening angles as small as $\omega \sim 10-30°$.

For the BBH stacking, the stacked limits in the nominal scenario ($\gamma = 2$ and isotropic emission) are $E^{\mathrm{iso}}_{\mathrm{tot},\nu} < 3.8 \times 10^{53}$ erg and $f_\nu < 0.14$, while the best limits from individual

GW name	Type	Distance	$\mathcal{R}_{90}$ area	Upper limits on neutrino emission		
				$E^2 \mathrm{d}N/\mathrm{d}E$	$E_{\mathrm{tot},\nu}^{\mathrm{iso}}$	f_ν^{iso}
		Mpc	deg^2	GeV cm^{-2}	erg	
GW191103_012549	BBH	927	2520	4.3×10^1	1.6×10^{56}	10.0×10^1
GW191105_143521	BBH	1141	730	1.5×10^2	6.3×10^{56}	4.3×10^2
GW191109_010717	BBH	1386	1784	1.2×10^1	1.2×10^{56}	1.8×10^1
GW191113_071753	BBH	1469	2993	3.1×10^1	3.7×10^{56}	3.0×10^2
GW191126_115259	BBH	1618	1514	1.1×10^2	8.0×10^{56}	4.2×10^2
GW191127_050227	BBH	3614	1499	2.1×10^1	1.8×10^{57}	2.5×10^2
GW191129_134029	BBH	774	851	1.5×10^1	3.6×10^{55}	2.7×10^1
GW191204_110529	BBH	1975	4747	4.6×10^1	8.9×10^{56}	2.8×10^2
GW191204_171526	BBH	637	365	8.6×10^0	1.2×10^{55}	6.8×10^0
GW191215_223052	BBH	1937	603	1.3×10^1	2.5×10^{56}	7.8×10^1
GW191216_213338	BBH	339	488	1.1×10^1	5.3×10^{54}	3.5×10^0
GW191219_163120	NSBH	569	2232	1.7×10^1	2.8×10^{55}	1.9×10^2
GW191222_033537	BBH	2991	2299	5.6×10^1	2.7×10^{57}	4.6×10^2
GW191230_180458	BBH	4296	1012	1.2×10^1	9.2×10^{56}	1.4×10^2
GW200105_162426	NSBH	266	7882	1.8×10^1	6.1×10^{54}	1.7×10^1
GW200112_155838	BBH	1248	4250	1.8×10^1	1.4×10^{56}	2.6×10^1
GW200115_042309	NSBH	298	519	6.8×10^0	2.8×10^{54}	1.2×10^1
GW200128_022011	BBH	3405	2677	1.8×10^2	7.6×10^{57}	1.4×10^3
GW200129_065458	BBH	883	87	8.8×10^0	2.8×10^{55}	5.4×10^0
GW200202_154313	BBH	411	160	5.4×10^0	3.2×10^{54}	2.4×10^0
GW200208_130117	BBH	2258	39	7.2×10^0	1.5×10^{56}	3.0×10^1
GW200208_222617	BBH	4547	1889	1.6×10^1	2.5×10^{57}	4.9×10^2
GW200209_085452	BBH	3447	925	2.5×10^2	2.2×10^{57}	4.5×10^2
GW200210_092255	NSBH	959	1830	2.3×10^1	8.6×10^{55}	1.9×10^2
GW200216_220804	BBH	3997	3010	7.8×10^0	6.5×10^{56}	1.0×10^2
GW200219_094415	BBH	3447	702	6.4×10^0	3.7×10^{56}	8.1×10^1
GW200220_061928	BBH	6321	3485	1.9×10^1	5.9×10^{57}	6.6×10^2
GW200220_124850	BBH	4172	3169	4.5×10^1	4.3×10^{57}	9.3×10^2
GW200224_222234	BBH	1677	51	1.3×10^1	1.5×10^{56}	2.4×10^1
GW200225_060421	BBH	1144	516	2.2×10^1	1.1×10^{56}	4.3×10^1
GW200302_015811	BBH	1545	7011	2.8×10^1	3.1×10^{56}	7.4×10^1
GW200306_093714	BBH	2228	4371	1.1×10^1	2.7×10^{56}	7.4×10^1
GW200308_173609	BBH	8867	18705	3.5×10^1	3.3×10^{58}	1.8×10^4
GW200311_115853	BBH	1152	37	1.7×10^1	8.7×10^{55}	1.8×10^1
GW200322_091133	BBH	8302	31571	3.6×10^1	3.0×10^{58}	4.9×10^4

Table 3. Same as table 1 for the events in the GWTC-3 catalogue [12].
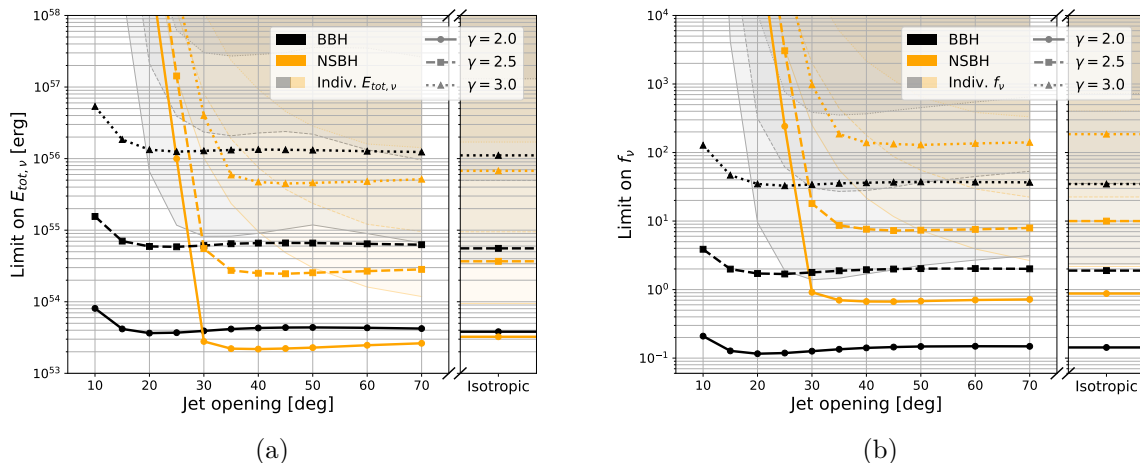
Figure 4. 90% upper limits on the per-source typical total energy emitted in neutrinos (left) and on f_ν (right) as a function of the jet opening angle (for von Mises model) and for the isotropic case (rightmost entry). The black (orange) curves correspond to the BBH (NSBH) stacking of mergers detected during O3. The different markers and line styles correspond to different spectral indices γ. The filled areas with the corresponding colours (merger category) and line styles (spectral index) indicate the envelope of the best individual upper limits.

follow-ups (for GW200202_154313) are respectively 3.2×10^{54} erg and 2.4. For the NSBH population, the corresponding limits are $E_{tot,\nu}^{iso} < 3.2 \times 10^{53}$ erg and $f_\nu < 0.88$, with the best individual limits being (for GW190814) 9.5×10^{53} erg and 2.2, respectively.

Finally, it is worth noticing that the statistical power of the BBH stacking already allows the exploration of reasonable values for f_ν (in the context of the assumed simple power-law spectrum), while all individual limits on this parameter are above 1, corresponding to a neutrino emission higher than the GW one.

Supplemental material with all numerical results for individual follow-ups and from the stacking analysis, for the various jet scenarios and assumed spectral indices, can be provided under request.

5 Discussion and conclusions

The search for neutrino counterparts to GW signals detected during the O3 run with the ANTARES detector yields no significant excess. This null result is used to extract upper limits on the neutrino emission, both in terms of the flux normalisation and of the total energy emitted in neutrinos, $E_{tot,\nu}^{iso}$, in particular for the standard case with an E^{-2} spectrum and isotropic emission.

The ANTARES analysis presented in this article benefits from the different event topologies in the detector, leading to all-flavour limits for neutrino energies above 100 GeV. The constraints are also interpreted in the context of population studies, for which limits can be put on the typical neutrino emission of different categories of sources (here, BBH and NSBH). As the most recent astrophysical models (e.g., [3, 27, 30]) seem to be out of reach for current detectors, such stacking studies may be one of the most promising approaches to identify joint emitters of neutrinos and GWs. More refined stackings may be studied by considering e.g., sub-populations among BBH mergers, such as the ones having similar source characteristics or environments.

The Bayesian analysis performed here considers flat priors, such that the stacking analysis is performed easily by multiplying the individual posterior distributions. Different priors (e.g., non-informative Jeffreys prior [31]) introduce correlations between the GW follow-ups and would only be possible by performing the posterior marginalisation over all GW events at once, therefore requiring more sophisticated integration techniques than the one employed in this paper.

First constraints on jetted emission for a von Mises model and for different spectral indices are derived as well. In the absence of the determination of any jet direction from the GW data or any electromagnetic observations, these results are only indirectly deducted from the stacking analysis. In future observation campaigns, any such measurement, even for one or a few sources, would allow for deriving direct constraints, as well as considering more complex jet models.

Though the ANTARES detector has been decommissioned in 2022, the KM3NeT experiment [32] has taken over the observation of the neutrino sky from the depths of the Mediterranean Sea. Data from the first few lines of KM3NeT/ORCA has already been used to perform an initial search for neutrino counterparts to the O3 events [33]. With more lines being deployed up to $\sim$ 2026, KM3NeT/ARCA and ORCA are expected to provide complementary coverage of the transient sky with respect to IceCube, increasing the chances to get significant individual detections and creating new opportunities for joint analyses.

The next GW observing period, O4, is expected to start in 2023, including the KAGRA detector in addition to LIGO and Virgo [34]. With an expected number of detections of the order of one hundred per year, population studies will become even more relevant.

Lastly, combinations with ZTF [35] or Vera C. Rubin [36] surveys and Target of Opportunity programs may help pinpoint candidate host galaxies for observed binary mergers, and allow more detailed analyses using the electromagnetic information and the environment characterisation as inputs for the prediction and constraint of the neutrino emission. More generally, there are still only a few models on the processes leading to neutrino production during binary merger events in the literature [3–5, 27, 30], and further theoretical developments in the coming years may bring new light to past, present, and future observations.

Acknowledgments

References

[1] LIGO Scientific and Virgo collaborations, *Observation of Gravitational Waves from a Binary Black Hole Merger*, *Phys. Rev. Lett.* **116** (2016) 061102 [arXiv:1602.03837] [InSPIRE].

[2] LIGO Scientific et al. collaborations, *Multi-messenger Observations of a Binary Neutron Star Merger*, *Astrophys. J. Lett.* **848** (2017) L12 [arXiv:1710.05833] [InSPIRE].

[3] S.S. Kimura et al., *Transejecta high-energy neutrino emission from binary neutron star mergers*, *Phys. Rev. D* **98** (2018) 043020 [arXiv:1805.11613] [InSPIRE].

[4] S.S. Kimura, K. Murase, P. Mészáros and K. Kiuchi, *High-Energy Neutrino Emission from Short Gamma-Ray Bursts: Prospects for Coincident Detection with Gravitational Waves*, *Astrophys. J. Lett.* **848** (2017) L4 [arXiv:1708.07075] [InSPIRE].

[5] K. Kotera and J. Silk, *Ultrahigh Energy Cosmic Rays and Black Hole Mergers*, *Astrophys. J. Lett.* **823** (2016) L29 [arXiv:1602.06961] [InSPIRE].

[6] ANTARES collaboration, *Search for neutrino counterparts of gravitational-wave events detected by LIGO and Virgo during run O2 with the ANTARES telescope*, *Eur. Phys. J. C* **80** (2020) 487 [arXiv:2003.04022] [InSPIRE].

[7] Baikal-GVD collaboration, *Search for High-Energy Neutrinos from GW170817 with the Baikal-GVD Neutrino Telescope*, *JETP Lett.* **108** (2018) 787 [arXiv:1810.10966] [InSPIRE].

[8] IceCube collaboration, *IceCube Search for Neutrinos Coincident with Gravitational Wave Events from LIGO/Virgo Run O3*, *Astrophys. J.* **944** (2023) 80 [arXiv:2208.09532] [InSPIRE].

[9] Super-Kamiokande collaboration, *Search for neutrinos in coincidence with gravitational wave events from the LIGO-Virgo O3a Observing Run with the Super-Kamiokande detector*, *Astrophys. J.* **918** (2021) 78 [arXiv:2104.09196] [InSPIRE].

[10] LIGO Scientific and Virgo collaborations, *GWTC-2: Compact Binary Coalescences Observed by LIGO and Virgo During the First Half of the Third Observing Run*, *Phys. Rev. X* **11** (2021) 021053 [arXiv:2010.14527] [InSPIRE].

[11] LIGO Scientific and VIRGO collaborations, *GWTC-2.1: Deep Extended Catalog of Compact Binary Coalescences Observed by LIGO and Virgo During the First Half of the Third Observing Run*, arXiv:2108.01045 [LIGO-P2100063] [InSPIRE].

[12] LIGO Scientific et al. collaborations, *GWTC-3: Compact Binary Coalescences Observed by LIGO and Virgo During the Second Part of the Third Observing Run*, arXiv:2111.03606 [LIGO-P2000318] [InSPIRE].

[13] LIGO Scientific et al. collaborations, *Observation of Gravitational Waves from Two Neutron Star-Black Hole Coalescences*, *Astrophys. J. Lett.* **915** (2021) L5 [arXiv:2106.15163] [InSPIRE].

[14] NASA/GSFC, *Flexible image transport system (fits)*, https://fits.gsfc.nasa.gov/ (2021).

[15] ANTARES collaboration, *ANTARES: the first undersea neutrino telescope*, *Nucl. Instrum. Meth. A* **656** (2011) 11 [arXiv:1104.1607] [InSPIRE].

[16] ANTARES collaboration, *A fast algorithm for muon track reconstruction and its application to the ANTARES neutrino telescope*, *Astropart. Phys.* **34** (2011) 652 [arXiv:1105.4116] [InSPIRE].

[17] ANTARES collaboration, *An algorithm for the reconstruction of neutrino-induced showers in the ANTARES neutrino telescope*, *Astron. J.* **154** (2017) 275 [arXiv:1708.03649] [ɪɴSPIRE].

[18] ANTARES collaboration, *All-sky search for high-energy neutrinos from gravitational wave event GW170104 with the Antares neutrino telescope*, *Eur. Phys. J. C* **77** (2017) 911 [arXiv:1710.03020] [ɪɴSPIRE].

[19] ANTARES et al. collaborations, *Search for High-energy Neutrinos from Binary Neutron Star Merger GW170817 with ANTARES, IceCube, and the Pierre Auger Observatory*, *Astrophys. J. Lett.* **850** (2017) L35 [arXiv:1710.05839] [ɪɴSPIRE].

[20] B. Baret et al., *Bounding the Time Delay between High-energy Neutrinos and Gravitational-wave Transients from Gamma-ray Bursts*, *Astropart. Phys.* **35** (2011) 1 [arXiv:1101.4669] [ɪɴSPIRE].

[21] C. Tamburini et al., *Deep-Sea Bioluminescence Blooms after Dense Water Formation at the Ocean Surface*, *PLoS One* **8** (2013) e67523.

[22] ANTARES collaboration, *Monte Carlo simulations for the ANTARES underwater neutrino telescope*, *JCAP* **01** (2021) 064 [arXiv:2010.06621] [ɪɴSPIRE].

[23] ANTARES collaboration, *First all-flavor neutrino pointlike source search with the ANTARES neutrino telescope*, *Phys. Rev. D* **96** (2017) 082001 [arXiv:1706.01857] [ɪɴSPIRE].

[24] ANTARES collaboration, *First search for neutrinos in correlation with gamma-ray bursts with the ANTARES neutrino telescope*, *JCAP* **03** (2013) 006 [arXiv:1302.6750] [ɪɴSPIRE].

[25] F. Folger, *Search for a diffuse cosmic neutrino flux using shower events in the ANTARES neutrino telescope*, Ph.D. Thesis, Friedrich-Alexander-Universität Erlangen-Nürnberg (2014) [ɪɴSPIRE].

[26] M. Bustamante and M. Ahlers, *Inferring the flavor of high-energy astrophysical neutrinos at their sources*, *Phys. Rev. Lett.* **122** (2019) 241101 [arXiv:1901.10087] [ɪɴSPIRE].

[27] M. Ahlers and L. Halser, *Neutrino Fluence from Gamma-Ray Bursts: Off-Axis View of Structured Jets*, *Mon. Not. Roy. Astron. Soc.* **490** (2019) 4935 [arXiv:1908.06953] [ɪɴSPIRE].

[28] R. Fisher, *Dispersion on a Sphere*, *Proc. R. Soc. A* **217** (1953) 295 [arXiv:1953.0064].

[29] D. Veske, Z. Márka, I. Bartos and S. Márka, *Neutrino emission upper limits with maximum likelihood estimators for joint astrophysical neutrino searches with large sky localizations*, *JCAP* **05** (2020) 016 [arXiv:2001.00566] [ɪɴSPIRE].

[30] V. Decoene et al., *High-energy neutrinos from fallback accretion of binary neutron star merger remnants*, *JCAP* **04** (2020) 045 [arXiv:1910.06578] [ɪɴSPIRE].

[31] H. Jeffreys, *An invariant form for the prior probability in estimation problems*, *Proc. Roy. Soc. Lond. A* **186** (1946) 453 [arXiv:1946.0056].

[32] KM3NeT collaboration, *Letter of intent for KM3NeT 2.0*, *J. Phys. G* **43** (2016) 084001 [arXiv:1601.07459] [ɪɴSPIRE].

[33] KM3NeT collaboration, *Search for neutrino counterparts from gravitational waves from the run O3 with KM3NeT*, in preparation (2023).

[34] KAGRA et al. collaborations, *Prospects for observing and localizing gravitational-wave transients with Advanced LIGO, Advanced Virgo and KAGRA*, *Living Rev. Rel.* **21** (2018) 3 [arXiv:1304.0670] [ɪɴSPIRE].

[35] E.C. Bellm et al., *The Zwicky Transient Facility: System Overview, Performance, and First Results*, *Publ. Astron. Soc. Pac.* **131** (2018) 018002.

[36] I. Andreoni et al., *Target-of-opportunity Observations of Gravitational-wave Events with Vera C. Rubin Observatory*, *Astrophys. J. Supp.* **260** (2022) 18 [arXiv:2111.01945] [ɪɴSPIRE].

The ANTARES collaboration

A. Albert,[a,b] S. Alves,[c] M. André,[d] M. Ardid,[e] S. Ardid,[e] J.-J. Aubert,[f] J. Aublin,[g] B. Baret,[g] S. Basa,[h] Y. Becherini,[g] B. Belhorma,[i] M. Bendahman,[g,j] F. Benfenati,[k,l] V. Bertin,[f] S. Biagi,[m] M. Bissinger,[n] J. Boumaaza,[j] M. Bouta,[o] M.C. Bouwhuis,[p] H. Brânzaş,[q] R. Bruijn,[p,r] J. Brunner,[f] J. Busto,[f] B. Caiffi,[s] D. Calvo,[c] S. Campion,[t,u] A. Capone,[t,u] L. Caramete,[q] F. Carenini,[k,l] J. Carr,[f] V. Carretero,[c] S. Celli,[t,u] L. Cerisy,[f] M. Chabab,[v] T.N. Chau,[g] R. Cherkaoui El Moursli,[j] T. Chiarusi,[k] M. Circella,[w] J.A.B. Coelho,[g] A. Coleiro,[g] R. Coniglione,[m] P. Coyle,[f] A. Creusot,[g] A.S.M. Cruz,[x] A.F. Díaz,[y] B. De Martino,[f] C. Distefano,[m] I. Di Palma,[t,u] A. Domi,[p,r] C. Donzaud,[g,z] D. Dornic,[f] D. Drouhin,[a,b] T. Eberl,[n] T. van Eeden,[p] D. van Eijk,[p] S. El Hedri,[g] N. El Khayati,[j] A. Enzenhöfer,[f] P. Fermani,[t,u] G. Ferrara,[m] F. Filippini,[k,l] L. Fusco,[aa] S. Gagliardini,[t,u] J. García,[e] C. Gatius Oliver,[p] P. Gay,[ab,g] N. Geißelbrecht,[n] H. Glotin,[ac] R. Gozzini,[c] R. Gracia Ruiz,[n] K. Graf,[n] C. Guidi,[s,ad] L. Haegel,[g] S. Hallmann,[n] H. van Haren,[ae] A.J. Heijboer,[p] Y. Hello,[af] J.J. Hernández-Rey,[c] J. Hößl,[n] J. Hofestädt,[n] F. Huang,[f] G. Illuminati,[k,l] C.W. James,[x] B. Jisse-Jung,[p] M. de Jong,[p,ag] P. de Jong,[p,r] M. Kadler,[ah] O. Kalekin,[n] U. Katz,[n] A. Kouchner,[g] I. Kreykenbohm,[ai] V. Kulikovskiy,[s] R. Lahmann,[n] M. Lamoureux,[g,1,2] A. Lazo,[c] D. Lefèvre,[aj,ak] E. Leonora,[al] G. Levi,[k,l] S. Le Stum,[f] D. Lopez-Coto,[am] S. Loucatos,[an,g] L. Maderer,[g] J. Manczak,[c] M. Marcelin,[h] A. Margiotta,[k,l] A. Marinelli,[ao] J.A. Martínez-Mora,[e] P. Migliozzi,[ao] A. Moussa,[o] R. Muller,[p] L. Nauta,[p] S. Navas,[am] E. Nezri,[h] B. Ó Fearraigh,[p] A. Păun,[q] G.E. Păvălaş,[q] M. Perrin-Terrin,[f] V. Pestel,[p] P. Piattelli,[m] C. Poirè,[e] V. Popa,[q] T. Pradier,[a] N. Randazzo,[al] D. Real,[c] S. Reck,[n] G. Riccobene,[m] A. Romanov,[s,ad] A. Sánchez-Losa,[c,w] A. Saina,[c] F. Salesa Greus,[c] D.F.E. Samtleben,[p,ag] M. Sanguineti,[s,ad] P. Sapienza,[m] J. Schnabel,[n] J. Schumann,[n] F. Schüssler,[an] J. Seneca,[p] M. Spurio,[k,l] Th. Stolarczyk,[an] M. Taiuti,[s,ad] Y. Tayalati,[j] S.J. Tingay,[x] B. Vallage,[an,g] G. Vannoye,[f] V. Van Elewyck,[g,ap] S. Viola,[m] D. Vivolo,[ao,aq] J. Wilms,[ai] S. Zavatarelli,[s] A. Zegarelli,[t,u] J.D. Zornoza[c] and J. Zúñiga[c]

[a] Université de Strasbourg, CNRS, IPHC UMR 7178, F-67000 Strasbourg, France
[b] Université de Haute Alsace, F-68100 Mulhouse, France
[c] IFIC — Instituto de Física Corpuscular (CSIC — Universitat de València) c/ Catedrático José Beltrán, 2 E-46980 Paterna, Valencia, Spain
[d] Technical University of Catalonia, Laboratory of Applied Bioacoustics, Rambla Exposició, 08800 Vilanova i la Geltrú, Barcelona, Spain
[e] Institut d'Investigació per a la Gestió Integrada de les Zones Costaneres (IGIC) — Universitat Politècnica de València. C/ Paranimf 1, 46730 Gandia, Spain
[f] Aix Marseille Univ, CNRS/IN2P3, CPPM, Marseille, France
[g] Université Paris Cité, CNRS, Astroparticule et Cosmologie, F-75013 Paris, France
[h] Aix Marseille Univ, CNRS, CNES, LAM, Marseille, France
[i] National Center for Energy Sciences and Nuclear Techniques, B.P. 1382, R.P. 10001 Rabat, Morocco
[j] University Mohammed V in Rabat, Faculty of Sciences, 4 av. Ibn Battouta, B.P. 1014, R.P. 10000 Rabat, Morocco
[k] INFN — Sezione di Bologna, Viale Berti-Pichat 6/2, 40127 Bologna, Italy
[l] Dipartimento di Fisica e Astronomia dell'Università di Bologna, Viale Berti-Pichat 6/2, 40127, Bologna, Italy
[m] INFN — Laboratori Nazionali del Sud (LNS), Via S. Sofia 62, 95123 Catania, Italy
[n] Friedrich-Alexander-Universität Erlangen-Nürnberg, Erlangen Centre for Astroparticle Physics, Erwin-Rommel-Str. 1, 91058 Erlangen, Germany
[o] University Mohammed I, Laboratory of Physics of Matter and Radiations, B.P. 717, Oujda 6000, Morocco
[p] Nikhef, Science Park, Amsterdam, The Netherlands
[q] Institute of Space Science, RO-077125 Bucharest, Măgurele, Romania
[r] Universiteit van Amsterdam, Instituut voor Hoge-Energie Fysica, Science Park 105, 1098 XG Amsterdam, The Netherlands
[s] INFN — Sezione di Genova, Via Dodecaneso 33, 16146 Genova, Italy

^{t} INFN — Sezione di Roma, P.le Aldo Moro 2, 00185 Roma, Italy

^{u} Dipartimento di Fisica dell'Università La Sapienza, P.le Aldo Moro 2, 00185 Roma, Italy

^{v} LPHEA, Faculty of Science — Semlali, Cadi Ayyad University,
P.O.B. 2390, Marrakech, Morocco

^{w} INFN — Sezione di Bari, Via E. Orabona 4, 70126 Bari, Italy

^{x} International Centre for Radio Astronomy Research — Curtin University,
Bentley, WA 6102, Australia

^{y} Department of Computer Architecture and Technology/CITIC, University of Granada,
18071 Granada, Spain

^{z} Université Paris-Sud, 91405 Orsay Cedex, France

^{aa} Università di Salerno e INFN Gruppo Collegato di Salerno, Dipartimento di Fisica,
Via Giovanni Paolo II 132, Fisciano, 84084 Italy

^{ab} Laboratoire de Physique Corpusculaire, Clermont Université, Université Blaise Pascal,
CNRS/IN2P3, BP 10448, F-63000 Clermont-Ferrand, France

^{ac} LIS, UMR Université de Toulon, Aix Marseille Université, CNRS, 83041 Toulon, France

^{ad} Dipartimento di Fisica dell'Università, Via Dodecaneso 33, 16146 Genova, Italy

^{ae} Royal Netherlands Institute for Sea Research (NIOZ),
Landsdiep 4, 1797 SZ 't Horntje (Texel), the Netherlands

^{af} Géoazur, UCA, CNRS, IRD, Observatoire de la Côte d'Azur, Sophia Antipolis, France

^{ag} Huygens-Kamerlingh Onnes Laboratorium, Universiteit Leiden, The Netherlands

^{ah} Institut für Theoretische Physik und Astrophysik, Universität Würzburg,
Emil-Fischer Str. 31, 97074 Würzburg, Germany

^{ai} Dr. Remeis-Sternwarte and ECAP, Friedrich-Alexander-Universität Erlangen-Nürnberg,
Sternwartstr. 7, 96049 Bamberg, Germany

^{aj} Mediterranean Institute of Oceanography (MIO), Aix-Marseille University,
13288 Marseille, Cedex 9, France

^{ak} Université du Sud Toulon-Var, CNRS-INSU/IRD UM 110, 83957 La Garde Cedex, France

^{al} INFN — Sezione di Catania, Via S. Sofia 64, 95123 Catania, Italy

^{am} Dpto. de Física Teórica y del Cosmos & C.A.F.P.E., University of Granada,
18071 Granada, Spain

^{an} IRFU, CEA, Université Paris-Saclay, F-91191 Gif-sur-Yvette, France

^{ao} INFN — Sezione di Napoli, Via Cintia 80126 Napoli, Italy

^{ap} Institut Universitaire de France, 75005 Paris, France

^{aq} Dipartimento di Fisica dell'Università Federico II di Napoli, Via Cintia 80126, Napoli, Italy

^{1} Also at INFN — Sezione di Padova, 35131 Padova, Italy

^{2} Now at Centre for Cosmology, Particle Physics and Phenomenology — CP3,
Université catholique de Louvain, Louvain-la-Neuve, Belgium